catalysts

MDPI

Article

Visible-Light-Driven BiOBr-TiO_2-Attapulgite Photocatalyst with Excellent Photocatalytic Activity for Multiple Xanthates

Yaozhong Qi, Sikai Zhao *, Xiaoyu Jiang, Zhangke Kang, Shuling Gao, Wengang Liu and Yanbai Shen *

School of Resources and Civil Engineering, Northeastern University, Shenyang 110819, China; yaozhongqi0928@163.com (Y.Q.); jangsdrl@163.com (X.J.); 2010408@stu.neu.edu.cn (Z.K.); gaoshuling@mail.neu.edu.cn (S.G.); liuwengang@mail.neu.edu.cn (W.L.)

* Correspondence: zhaosikai@mail.neu.edu.cn (S.Z.); shenyanbai@mail.neu.edu.cn (Y.S.)

Abstract: The novel ternary composites BiOBr-TiO_2-attapulgite (BTA) were synthesized using a simple hydrothermal and water-bath method, exhibiting excellent photocatalytic performance to multiple xanthates. For the BTA photocatalyst, TiO_2 and BiOBr were uniformly loaded onto the surface of acid-activated attapulgite. As a widely used collector in mining processes, sodium ethyl-xanthate (SEX) was selected as the target pollutant due to its high toxicity. The BTA ternary photocatalyst demonstrated significantly higher adsorption and photocatalytic degradation performance compared to TiO_2 nanoparticles, BiOBr nanosheets, and BiOBr-TiO_2 heterojunction. Structural characterization and experimental results indicated that the exceptional photocatalytic degradation efficiency of BTA was mainly attributed to the formation of a heterojunction between BiOBr and TiO_2, as well as the presence of additional active adsorption sites provided by attapulgite. Free radical scavenging experiments and EPR results confirmed that the photogenerated holes were the predominant active species in photodegrading SEX throughout the entire experiment. The LC-MS results provided insight into potential degradation pathways of SEX. This research demonstrates that BTA, as a novel triple composite material, achieves rapid and complete degradation to 20 mg/L SEX within 20 min. This work presents a novel approach to synthesize mineral-based photocatalysts, which have broad prospects for application in flotation wastewater treatment.

Keywords: BiOBr-TiO_2-attapulgite; ternary composites; photocatalysis; visible light; xanthates

Citation: Qi, Y.; Zhao, S.; Jiang, X.; Kang, Z.; Gao, S.; Liu, W.; Shen, Y. Visible-Light-Driven BiOBr-TiO_2-Attapulgite Photocatalyst with Excellent Photocatalytic Activity for Multiple Xanthates. *Catalysts* **2023**, *13*, 1504. https://doi.org/10.3390/catal13121504

Academic Editor: Detlef W. Bahnemann

Received: 14 November 2023
Revised: 6 December 2023
Accepted: 8 December 2023
Published: 10 December 2023

1. Introduction

With the advancement of mining operations, flotation has become an indispensable process in ore dressing, resulting in the production of a significant volume of flotation wastewater that has the potential to contaminate the natural environment [1,2]. Xanthate, due to its cost-effectiveness and outstanding flotation capabilities, has emerged as a crucial collector for sulfide minerals and gold ores [3]. Although a substantial amount of xanthate is consumed during the flotation process, there is still a considerable presence of xanthate in the wastewater, ranging from 5 to 40 mg/L [4]. Such a high concentration of xanthate can result in the rapid mortality of nearly all fish in a few days, leading to significant environmental issues [5,6]. It also threatens the local economy and the food security of the region. Furthermore, Xanthate poses significant dangers to human livers, blood, and nervous systems [7]. Especially, the decomposition of xanthate will generate CS_2 gas, which irreversibly damages the respiratory system [8]. In order to highly reduce the hazards released by xanthate-containing wastewater, some proactive and effective measures should be implemented.

Photocatalysis, as one of the advanced oxidation processes (AOPs), is popular owing to its high efficiency, environmental friendliness, and sustainability [9]. Up to now, the extensive research of photocatalytic degradation technology for the treatment of xanthate-containing wastewater has been carried out to mitigate pollution [10]. The utilization of

light energy for catalyzing the degradation of xanthate-containing wastewater enables the achievement of water management and purification objectives [10,11].

Titanium dioxide (TiO_2) is a commonly employed semiconductor material in photocatalysis, renowned for its responsiveness to ultraviolet light, stability, cost-effectiveness, and environmental friendliness [12]. Nonetheless, the photocatalytic performance of single TiO_2 (T) faces some limitations, such as agglomeration by high surface energy, wide bandgap, low response to visible light, and a rapid recombination of e^-/h^+ pairs [13]. To address these challenges, the effective strategies involve the use of appropriate carriers and the creation of heterostructures with other semiconductors. These strategies aid in mitigating TiO_2 agglomeration, suppressing the recombination of electron–hole pairs, improving the efficiency of visible light utilization, and ultimately enhancing the photocatalytic efficiency under visible light [14,15].

Coupling TiO_2 on the surface of a carrier can effectively improve the dispersibility of TiO_2 [16,17]. So far, significant attention has been given to employing clay minerals as a catalytic substrate to reduce production costs and to disperse catalysts [18]. Attapulgite (A) is a layered silicate mineral with a nanoporous structure, which can effectively inhibit particle aggregation and increase active sites [17,19]. Due to its chemical inertness, resistance to deterioration, and cost-effectiveness for large-scale commercialization, attapulgite is widely used in various industrial, catalytic, and environmental applications [20]. Therefore, attapulgite-supported TiO_2 can form composite catalysts with a large number of active sites, raising the contact frequency between the catalyst and pollutants, and thus enhancing photocatalytic activity [20–22].

To address the wide bandgap of TiO_2 (~3.0 eV), the formation of a heterojunction can further effectively reduce the bandgap width, prevent the recombination of electron–hole pairs, and thus generate more active species for enhancing the photocatalytic activity [23]. Due to its narrower bandgap compared with TiO_2, BiOBr (B) can absorb visible light and enhance the visible light activity of photocatalyst. As a typical two-dimensional semiconductor material, BiOBr has a tetragonal matlockite structure comprising alternating layers of $[Bi_2O_2]^{2+}$ and Br^-, exhibiting excellent crystallinity, forming highly crystalline nanosheets that maintain their integrity throughout the photocatalytic process [24,25]. The electric field generated within the structure facilitates the separation of photo-generated charge carriers, consequently enhancing the photocatalytic activity. Additionally, it has been observed that tight coupling heterojunctions through chemical bonding can establish efficient charge transfer pathways, thus greatly reducing photo-induced carrier recombination [26]. The construction of a BiOBr/TiO_2 (BT) type II heterojunction, with TiO_2 acting as the primary catalyst and BiOBr as the co-catalyst, can prolong the transfer distance and separation time of e^-/h^+ pairs, enable the utilization of the visible light spectrum, and considerably enhance the efficiency of visible light utilization [27–29].

The BiOBr-TiO_2-attapulgite (BTA) composites were synthesized through a hydrothermal and water-bath method in this study. Xanthates were selected as the target pollutants because they are highly toxic and their release into ecosystems poses a severe threat to human health and significant environmental problems. The application parameters of the photocatalyst were investigated to determine the optimal conditions for xanthate degradation. The characterization results and experimental data were used to propose potential photocatalytic degradation pathways and mechanisms.

2. Results and Discussion

2.1. Characterization of Materials

2.1.1. Phase Analysis

X-ray diffraction (XRD) analysis can determine the crystalline structure of materials by identifying their corresponding diffraction peaks. In Figure 1a, it can be seen that the diffraction peaks located at 25.28°, 36.95°, and 48.05° are well matched with the crystal planes (101), (103), and (200) of anatase TiO_2 (JCPDS No. 21-1272) [30]. The XRD patterns also exhibit peaks at 10.90°, 21.93°, and 31.69°, which correspond to the crystal planes (001),

(002), and (102) of BiOBr (JCPDS No. 09-0393) [31]. Moreover, the presence of attapulgite (JCPDS No. 00-021-0550) is confirmed by the peaks at 13.90°, 19.85°, 26.7°, and 35.32°, which can be attributed to its crystal planes [32]. Furthermore, the distinct peaks observed at 10.90° and 31.69° in the BT composites (Figure 1b) are in good agreement with the crystal planes of BiOBr, while the remaining diffraction peaks are consistent with the crystal planes of anatase TiO_2. Compared to BT, the diffraction peaks of BTA remain largely unchanged, with weak peaks observed at 26.7° and 35.32°. This suggests that the attapulgite has no significant impact on the interaction between BiOBr and TiO_2. Moreover, the presence of these two additional weak peaks indicates the successful loading of BiOBr and TiO_2 onto attapulgite.

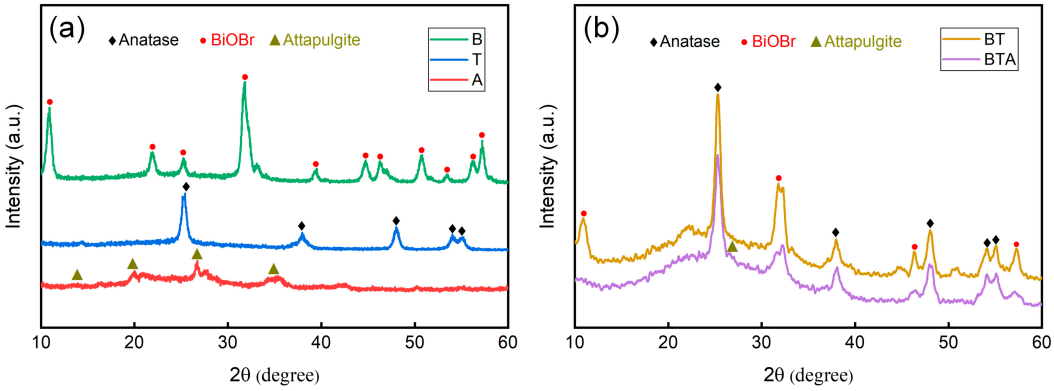

Figure 1. XRD patterns of (**a**) B, T, A and (**b**) BT, BTA samples.

2.1.2. Morphology Analysis

The morphology, microstructure and element distribution of samples are observed through scanning electron microscopy (SEM), transmission electron microscopy (TEM), and energy dispersive spectrum (EDS). Figure 2a,b show severe aggregation of nanostructured TiO_2 and BiOBr particles, which can be attributed to their high surface energy. Individual TiO_2 particles are approximately 20~25 nm in size (Figure 2a). BiOBr is a representative two-dimensional material with dimensions ranging from approximately 200 to 400 nm in length and 6 nm in thickness (Figure 2b). The attapulgite presents a distinctive layered chain with fibrous aggregation morphology, facilitating the assembly of TiO_2 and BiOBr (Figure 2c). In Figure 2d, BiOBr firmly adheres to the surface of TiO_2 to form BT binary composites, which can promote electron transfer through an increased contact area and thus improve catalytic reaction efficiency. Figure 2e demonstrates that the dispersion of TiO_2 and BiOBr in the BTA ternary heterogeneous system is notably improved when attapulgite is employed as a carrier. Combined with BET results (Table S1), the incorporation of attapulgite markedly enhances the specific surface area of BT composites, exceeding the dispersion achieved by BT binary materials. BTA effectively weakens the aggregation of BiOBr and TiO_2, resulting in the formation of ternary composites characterized by intimate contact and prominently exposed edges. This expands the contact area of photocatalysts with the target degradation substance and thus greatly enhances photocatalytic activity. Figure 2f presents a TEM image of BTA, exhibiting a close combination of attapulgite, TiO_2, and BiOBr, which is in good agreement with the SEM image. The SAED pattern (Figure 2g) displays the concentric rings of BTA, and this can be indexed to the planes of anatase TiO_2 [3,33]. In the HRTEM image (Figure 2h), the lattice fringe spacings of BiOBr and TiO_2 are determined to be approximately 0.19 and 0.35 nm, corresponding to the (201) and (101) crystal planes of BiOBr and anatase TiO_2, respectively [3,34]. An EDS analysis (Figure S1) identifies the primary elements in BTA as Bi, O, Br, Ti, and Si. The elemental mappings from Figure 2i–m demonstrate the uniform distribution of all elements within the composites. The results indicate a uniform coexistence and distribution of BiOBr, anatase TiO_2, and attapulgite.

The analysis further verifies the even distribution of anatase TiO_2 nanoparticles and BiOBr nanosheets on the surface of attapulgite.

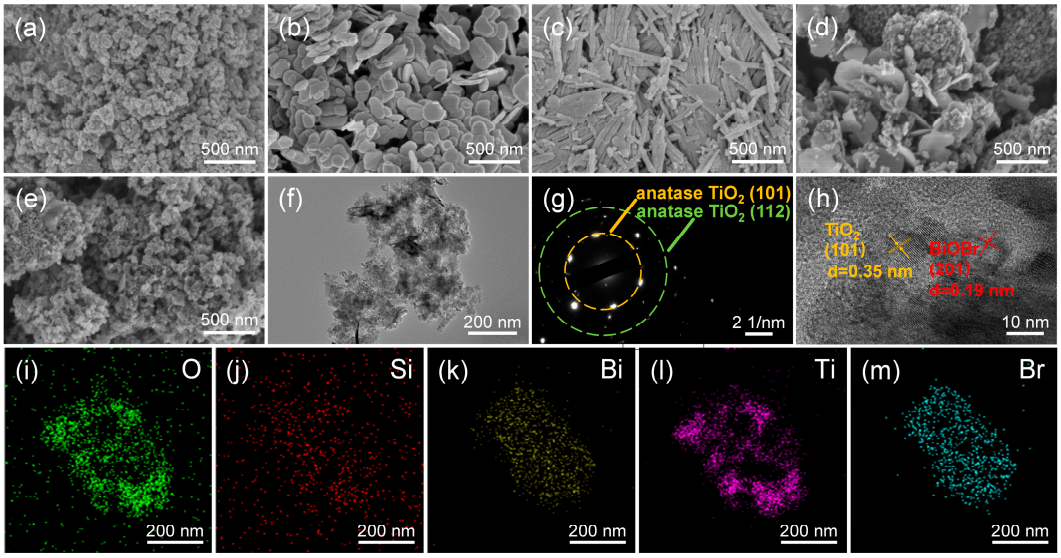

Figure 2. SEM images of (**a**) T, (**b**) B, (**c**) A, (**d**) BT, and (**e**) BTA. (**f**) TEM image, (**g**) SAED pattern, (**h**) HRTEM image, and (**i**–**m**) element mappings of BTA composites.

2.1.3. Surface Chemical State Analysis

Figure 3 illustrates the elemental composition and binding states of BTA ternary composites using an XPS analysis.

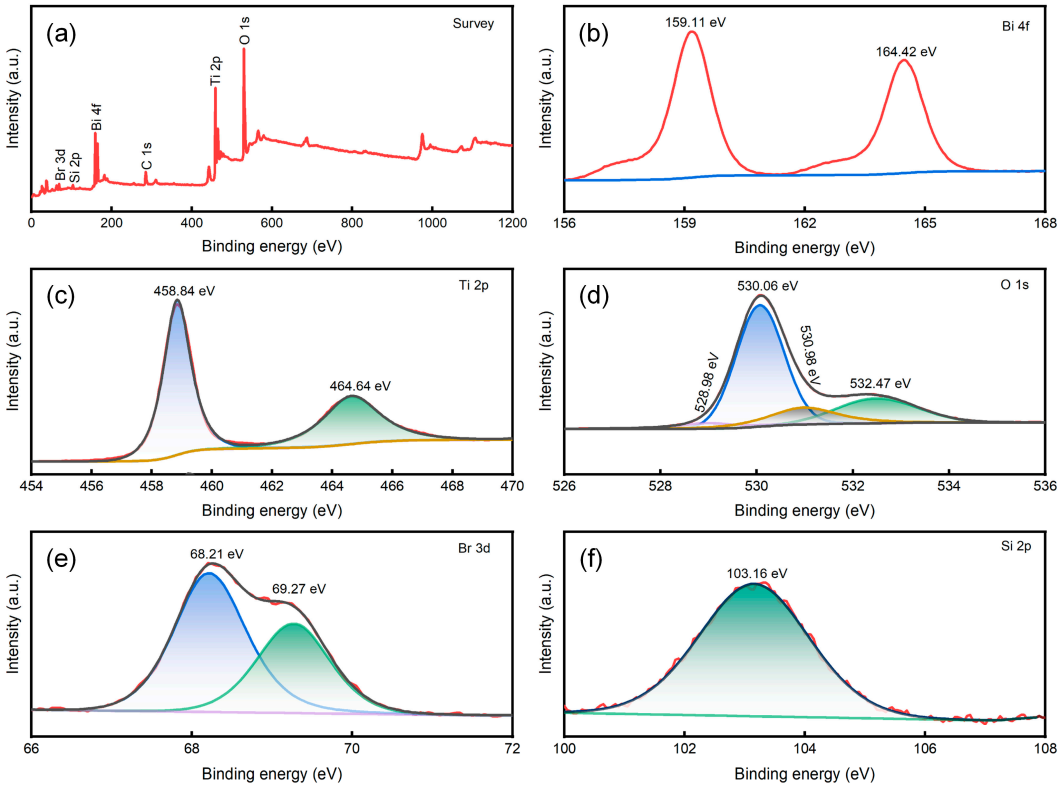

Figure 3. XPS spectra of BTA composites. (**a**) Survey scan; (**b**) Bi 4f; (**c**) Ti 2p; (**d**) O 1s; (**e**) Br 3d; (**f**) Si 2p.

Based on the complete spectrum displayed in Figure 3a, the BTA ternary composites predominantly consist of five elements, namely Bi, Br, O, Ti, and Si. This shows that the main components of BTA are BiOBr, TiO_2, and attapulgite. The peaks positioned at 159.11 and 163.42 eV in Figure 3b correspond to Bi $4f_{7/2}$ and Bi $4f_{5/2}$, respectively, indicating the presence of characteristic peaks associated with Bi^{3+} in BiOBr [35]. It is worth noting that two weak peaks appear at Bi 4f, approximately 157.5 and 62.8 eV, which may be due to the formation of a small amount of $Bi_{24}O_{31}Br_{10}$ during high-temperature calcination [36]. In Figure 3c, the XPS spectra of Ti 2p exhibit peaks at 458.84 and 464.64 eV, which correspond to the normal state of Ti $2p_{3/2}$ and Ti $2p_{1/2}$ of Ti^{4+} in TiO_2 [2]. The XPS spectrum of O 1s is presented in Figure 3d, revealing the presence of O in four distinct binding modes. The four peaks at 528.98, 530.06, 530.98, and 532.47 eV represent $[Bi_2O_2]^{2+}$, Ti-O-Ti, surface -OH groups, and Si-O-Si, respectively [3]. In Figure 3e, two peaks are observed at 68.21 and 69.27 eV, corresponding to Br $3d_{5/2}$ and Br $3d_{3/2}$, respectively, suggesting the presence of Br^{-1} in BiOBr [37]. The Si 2p spectrum shown in Figure 3f is observed at 103.16 eV, indicating the presence of SiO_2 in attapulgite [38]. The XPS results provide additional evidence for the strong incorporation of BiOBr and TiO_2 into the attapulgite carrier, indicating a more comprehensive integration rather than mere mixing.

2.1.4. TG-DSC Analysis

Thermogravimetric and differential scanning calorimetry (TG-DSC) curves in Figure 4 are used to describe the mass change in BTA composites with increasing temperature [39,40]. Evaporation, phase transition, and chemical reactions are the primary factors contributing to the decrease in sample mass. Below 270.3 °C, the 3.94% decrease in mass of BTA composites is primarily attributed to the loss of water adsorbed on its surface. With a further increase in temperature up to 477.6 °C, there is an approximate 1.29% in mass loss, resulting from the evaporation of structural water in attapulgite. The increase in progressive temperature leads to an approximately 11.27% loss in mass with an exothermic process, signifying the formation of new substances. Herein, this process is likely to involve the decomposition of BiOBr under high-temperature conditions, yielding $Bi_{24}O_{31}Br_{10}$ and Br_2 gas, resulting in heat release and mass loss [41]. The analysis of TG-DSC curves highlights the significance of selecting an optimal calcination temperature to achieve a good photocatalytic performance in BTA ternary materials.

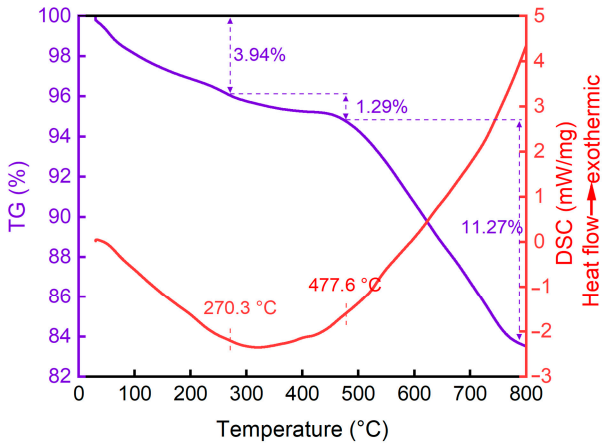

Figure 4. TG-DSC curves of BTA composites.

2.2. Photocatalytic Activity

The synthesis conditions have important influence on the performance of the photocatalyst. In our previous study, we optimized the ratio of BiOBr and TiO_2 [42]. Additionally, the comparison of photocatalytic performance of various doses of attapulgite with BT significantly influences the photocatalyst, as illustrated in Figure 5a,b. As the quantity of attapulgite increased gradually, the degradation efficiencies of BTA-1, BTA-2, and BTA-3

reached 84.1%, 94.8%, and 51.31%, respectively, after a 20 min photocatalytic degradation reaction. The performance of the photocatalyst initially increases and then decreases, with BTA-2 achieving the maximum catalytic efficiency. Furthermore, in the comparison of the first-order kinetic reaction constant, BTA-2 is higher than both BTA-1 and BTA-3, at 0.11699 min^{-1}. Therefore, BTA-2 is utilized as the optimal condition for the application test. For simplicity, BTA will represent BTA-2 in the rest of the section.

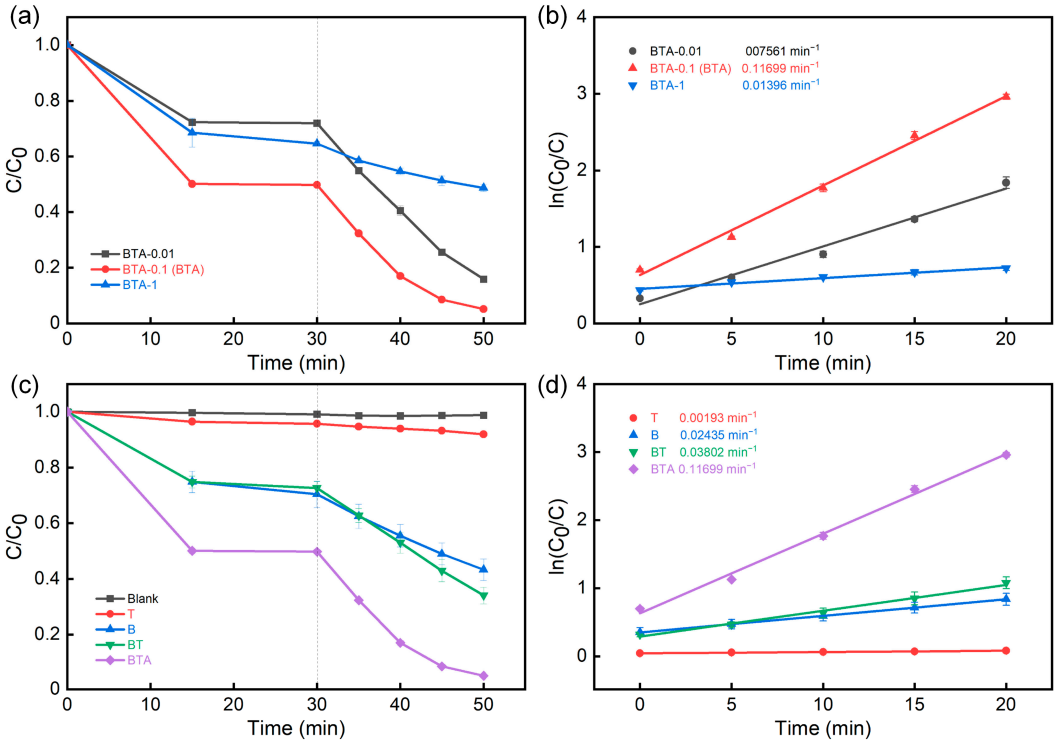

Figure 5. (**a**) Degradation efficiency curves and (**b**) kinetic curves of BTA-0.01, BTA, and BTA-1 to 20 mg/L SEX. (**c**) Degradation efficiency curves and (**d**) kinetic curves of Blank, T, B, BT, and BTA to 20 mg/L SEX.

Figure 5c,d compare the degradation efficiency curves and kinetic curves of different samples of TiO_2, BiOBr, BT, and BTA to SEX, aiming to demonstrate the robust photocatalytic performance of BTA. The experiment employed a visible light intensity of 400 W, an SEX initial concentration of 20 mg/L, and a catalyst dosage of 0.2 g/L. Based on Figure 5c, the adsorption of SEX by photocatalysts reaches dynamic equilibrium within 30 min of the dark reaction. Compared to the other samples, BTA ternary composites exhibit significantly enhanced adsorption performance to SEX. This improvement can be ascribed to the addition of attapulgite weakening the aggregation of TiO_2 and BiOBr, significantly increasing the availability of active sites for SEX attachment. In contrast, TiO_2 demonstrates negligible photodegradation efficiency to SEX under visible light, indicating limited utilization of visible light and capability to degrade SEX, while BiOBr and BT exhibit more pronounced degradation performance to SEX and BT demonstrates higher degradation efficiency compared to BiOBr. This observation suggests that the formation of heterogeneous structures between TiO_2 and BiOBr can effectively improve the overall photocatalytic performance. BTA ternary composites exhibit a remarkable enhancement in photocatalytic degradation efficiency, with a first-order reaction rate constant of 0.11699 min^{-1}, which is approximately 3.1 times higher than that of BT. Such a finding suggests that the generation of more active sites on the surface of BTA composites promotes not only increased adsorption of SEX molecules but also rapid progress in the photocatalytic degradation reaction.

To effectively serve future industrial applications, it is imperative to carefully select suitable conditions and parameters for photocatalytic applications. The applicability of

BTA composites was thoroughly evaluated by examining the dosage of photocatalysts, concentration of xanthate, applicable pH range of wastewater, feasibility of degradation of various xanthates, and stability of photocatalysts.

Figure 6 shows that there was no significant change in the adsorption of SEX by any of the samples at 15 and 30 min of dark adsorption, suggesting that all samples achieved adsorption equilibrium within 30 min. Figure 6a,b illustrate the degradation efficiency curves and kinetic curves of BTA composites with different dosages to 20 mg/L SEX. In the experiment, a 50 mL solution of SEX was served as the reaction medium. The dosage of BTA composites was the only variable, systematically set at 0.10, 0.15, 0.20, 0.25, and 0.30 g/L. With the increase in photocatalyst dosage, the adsorption performance gradually increases and reaches adsorption–desorption dynamic equilibrium within 30 min. Over the course of the photocatalytic stage, the degradation effect of SEX intensifies with time, while the photocatalytic rate initially increases and then subsequently decreases with increasing photocatalyst dosage. As the dosage of the photocatalyst is raised from 0.10 to 0.20 g/L, the degradation rate of SEX increases due to the augmented number of catalytic sites in the ternary materials. Nonetheless, when the photocatalyst dosage further increases from 0.20 to 0.30 g/L, the catalytic rate begins to decelerate, possibly as a result of the excessive BTA photocatalyst obstructing visible light and diminishing its intensity. Consequently, for the treatment of xanthate-containing wastewater with a concentration of 20 mg/L, the BTA dosage ranging from 0.15 to 0.30 g/L can attain a photocatalytic degradation efficiency exceeding 90%. Obviously, the BTA dosage of 0.20 g/L exhibits the highest reaction rate in the degradation of SEX. Hence, such a photocatalyst dosage is selected as the optimal condition for subsequent optimization.

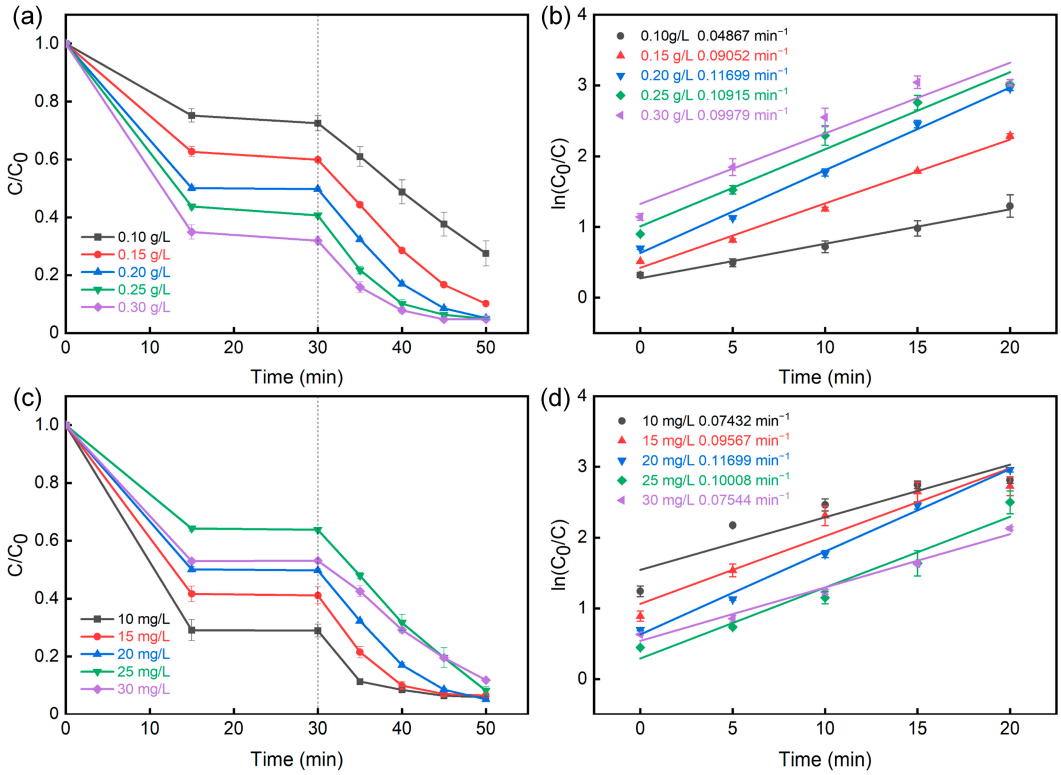

Figure 6. (**a**) Degradation efficiency curves and (**b**) kinetic curves of BTA composites with different dosages to 20 mg/L SEX. (**c**) Degradation efficiency curves and (**d**) kinetic curves of 0.20 g/L BTA composites to various initial concentrations of SEX.

The concentration of xanthate in discharged wastewater is typically around 10–30 mg/L [4]. Therefore, in this section, simulative mineral wastewater with a xanthate concentration of 10–30 mg/L was used for the investigation, and the corresponding results of the photocat-

alytic degradation of BTA composites are presented in Figure 6c,d. As the SEX concentration increases from 10 to 25 mg/L, the photocatalyst exhibits a decreasing trend in adsorption performance and the first-order reaction kinetic constant representing the photocatalytic performance. However, it is worth noting that when the SEX concentration increases to 30 mg/L, there is a slight enhancement observed in the adsorption performance of BTA composites. The main reason for this phenomenon is that, under the condition of keeping the active adsorption sites of BTA unchanged, the excess of SEX molecules enhances the likelihood of attaching to the surface of BTA composites. Within the SEX concentration ranging from 10 to 30 mg/L, all of the degradation efficiencies are around 90%, indicating that 0.20 g/L of BTA demonstrates outstanding degradation performance in practical applications. With increasing SEX concentration, the rate of photocatalytic degradation initially increases and subsequently decreases. The fastest photocatalytic degradation rate, achieving a degradation efficiency of 94.8%, is observed at a SEX concentration of 20 mg/L. Taking into account the subsequent experimental conditions, 20 mg/L of xanthate is chosen as the optimal condition to achieve the best degradation rate of SEX.

It is widely acknowledged that pH plays a crucial role in determining the surface charge of photocatalysts and the composition of pollutants, thereby exerting a profound influence on their photodegradation efficiency. Figure 7 demonstrates the degradation performance of 20 mg/L SEX under different pH conditions with and without 0.20 g/L of BTA composites. With the pH changes from 5 to 11, minimal SEX self-decomposition occurs in the wastewater system without photocatalysts. However, when BTA composites are introduced, an impressive degradation efficiency of approximately 90% is achieved within a narrower pH ranging from 5 to 9 (around 7.45 without any pH adjustment). Nevertheless, it should be noted that once the pH value exceeds 11, the catalytic activity towards wastewater degradation by this photocatalyst diminishes significantly. This phenomenon could potentially arise from either a decline in active oxygen groups generated by BTA composites under alkaline conditions. Consequently, in practical wastewater treatment processes, BTA composites could rapidly and effectively degrade SEX molecules within a pH range of 5 to 9.

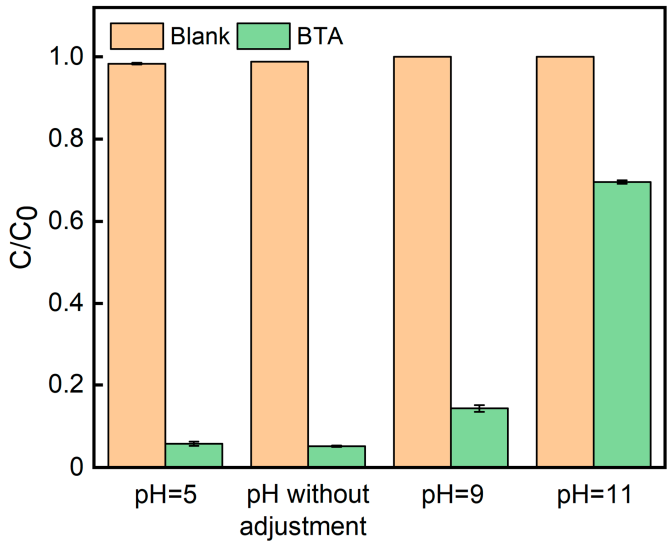

Figure 7. Degradation efficiency of 20 mg/L SEX at different pH values with and without 0.20 g/L of BTA composites.

Due to the widespread mixed usage of different types of xanthates in mining plants, Figure 8 illustrates the degradation efficiencies of various xanthates with a concentration of 20 mg/L under visible light conditions using 0.20 g/L of BTA composites. The adsorption capacity of BTA composites for different types of xanthates is correlated with the length of their side chains. This phenomenon can be attributed to the fact that longer-chain

xanthate molecules exhibit a stronger adhesion characteristic because of their relatively complex spatial structure, thus increasing their likelihood of adhering to the surface sites of BTA composites. Twenty minutes later, the degradation rates of SEX, SBX, SIPX, and SIAX reach 94.8%, 95.2%, 89.4%, and 97.3%, respectively. Therefore, it can be inferred that BTA composites universally degrade xanthates, confirming the compatibility of BTA with complex xanthate compositions in mining wastewater.

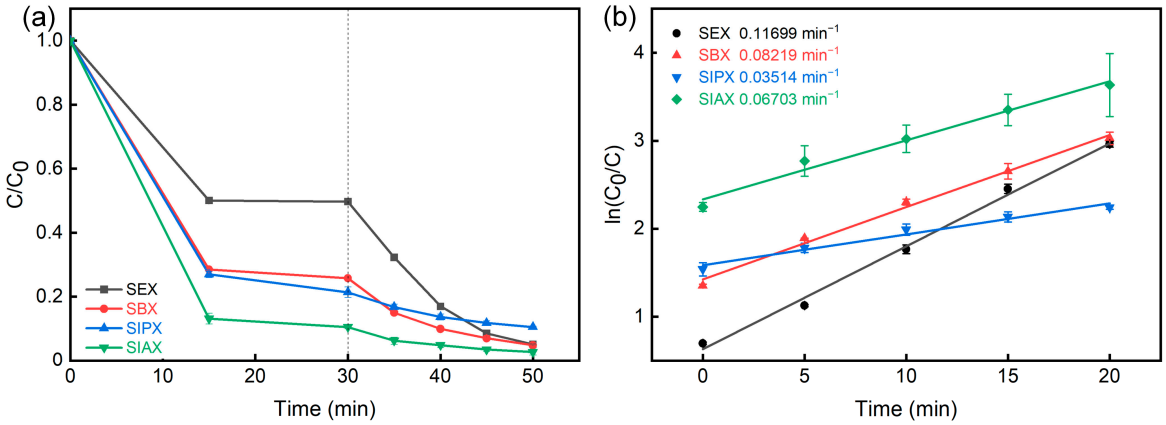

Figure 8. (**a**) Degradation efficiency curves and (**b**) kinetic curves of 0.20 g/L BTA composites with different types of xanthates.

In practical applications, the stability of photocatalysts is of great importance. Figure 9 demonstrates the microstructure changes in the BTA ternary photocatalyst by presenting XRD patterns and SEM images before and after the photocatalytic degradation process, along with an assessment of its long-term stability and reusability. From the XRD patterns shown in Figure 9a, it is found that BTA composites exhibit minimal changes before and after the reaction, indicating that the catalytic process does not disrupt the original lattice parameters. The SEM images in Figure 9b,c clearly illustrate that the post-reaction BTA composites maintain a distinct outline, in which TiO_2 nanoparticles are visibly presented, while BiOBr nanosheets remain a supporter on TiO_2. Consequently, the morphology of attapulgite is not revealed due to encapsulation by TiO_2. This implies that the morphology of BTA composites does not undergo significant alterations. In the long-term stability test, as shown in Figure 9d, the freshly prepared composites exhibit a photocatalytic degradation efficiency of 94.9%. Over a 30-day period, the degradation efficiency shows no significant change and remains above 90%, suggesting that BTA composites are suitable for long-term storage and practical applications. Additionally, Figure 9e illustrates the reusability of the BTA photocatalyst. A single photocatalytic process involves 30 min of dark adsorption followed by 20 min of photocatalytic reaction. As the number of cycles increases, the adsorption of SEX molecules by BTA composites decreases. A possible reason is that a small quantity of SEX molecules and intermediate products persist on the surface of the BTA photocatalyst after the completion of the reaction, thus reducing the adsorption sites of photocatalyst. After three cycles, the degradation rate of xanthate by BTA composites still exceeds 90%, showing that an excellent degradation efficiency is maintained. This observation highlights the ability of the multi-photocatalytic process to maintain the structure and heterojunction of BTA without disruption. Overall, it provides a valuable guideline for the long-term stability and efficient recycling ability of BTA photocatalysts in practical applications.

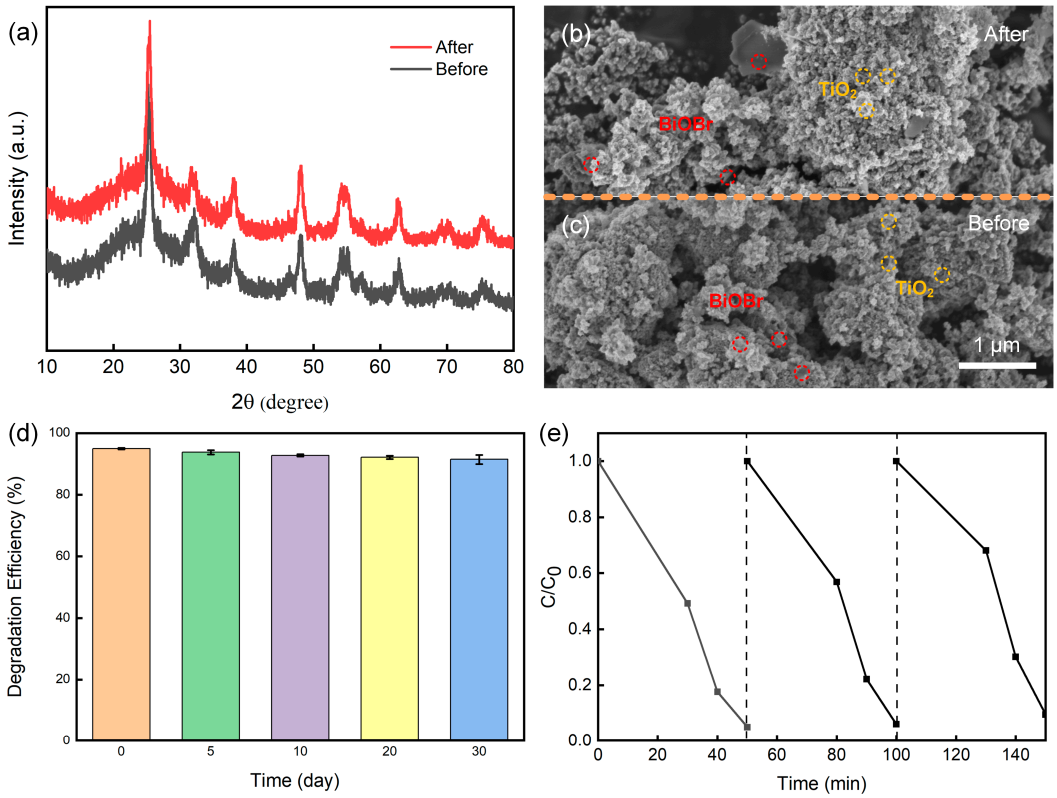

Figure 9. (**a**) XRD patterns and (**b**,**c**) SEM images of BTA composites before and after photocatalytic degradation reaction. (**d**) Long-term stability and (**e**) recycling performance of BTA composites.

To demonstrate the superior performance of BTA, Table 1 provides a comparison with previous works. BTA accomplishes complete degradation of xanthate within 20 min using an Xe lamp, while the degradation rate of other catalysts exceeds 100 min using the same light sources. Compared to catalyst utilizing a higher-energy mercury lamp, BTA achieves a quicker and more efficient complete degradation of SEX, thus confirming efficient photocatalytic degradation of BTA.

Table 1. Comparison of the degradation efficiency of previously reported photocatalysts used for photocatalytic degradation of xanthates.

Photocatalyst	Light Sources	Pollutants	Dosage (mg/L)	Degradation Rate	Irradiation Time (min)	Ref.
TiO_2/clinoptilolite	Mercury lamp	SIPX	20	Over 90%	30	[6]
BiOBr/g-C_3N_4	Xe lamp	SEX	30	96.1%	120	[8]
Ag/TiO_2/clinoptilolite	Xe lamp	SIPX	20	Approx. 60%	180	[11]
BiOCl/TiO_2/clinoptilolite	Xe lamp	SIPX	20	91.2%	180	[3]
BTA	Xe lamp	SEX	20	94.8%	40	This work

2.3. Possible Degradation Mechanism

In order to further explore the possible photodegradation pathway of SEX molecules, liquid chromatography–mass spectrometry (LC-MS) was used to analyze the content of simulated wastewater after photocatalysis for 5 min, and the results are shown in Figure S2. Based on the value of m/z, four possible intermediates are assumed: $CH_3O_2S_2^-$ (m/z = 112.1), $C_2H_5O_2S_2^-$ (m/z = 126.2), $C_2H_5O_2S_2^-$ (m/z = 141.1), and $C_4H_5OS_4^-$ (m/z = 198.1 and 199.1). The specific chemical structures of the intermediates are presented in Table S2. By analyzing real-time absorbance changes, conducting free radical activity tests, and examining the LC-MS results, the potential degradation pathways of SEX are provided

in Figure 10. The BTA photocatalyst generates a significant number of photogenerated holes, thereby leading to the strong oxidation of SEX molecules to $CH_3O_2S_2^-$, $C_2H_5O_2S_2^-$, $C_2H_5O_2S_2^-$, and $C_4H_5OS_4^-$, etc. This indicates that SEX and the intermediate products are eventually decomposed into smaller inorganic molecules, including CO_2, H_2O, and SO_4^{2-}, through continuous oxidation by free radicals.

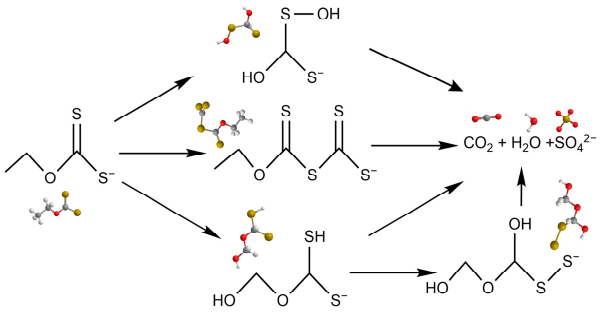

Figure 10. Possible degradation pathway of SEX.

To investigate the synergistic degradation effect of xanthate by different free radicals, a free radical trapping experiment was conducted. $AgNO_3$ solution (1 mL, 0.02 mol/L), p-benzoquinone (BQ, 5 mg), isopropyl alcohol (IPA, 1 mL) and EDTA-2Na (5 mg) are selected to trap e^-, $\cdot OH$, $\cdot O_2^-$, and h^+ radicals, respectively. As shown in Figure 11a, the addition of EDTA-2Na leads to a significant decrease in the degradation efficiency of SEX, reducing it to 7.9%. BQ addition also exhibits a certain effect with a reduction in degradation efficiency by 19.1%. However, the presence of IPA and $AgNO_3$ solution minimally impact the catalytic efficiency. These experiments highlight the dominant role of h^+ radicals as active species in the oxidative decomposition of xanthate molecules. In order to elucidate the predominant role of photogenerated holes in the reaction process and the mechanism of electron–hole pair separation, TEMPO is employed for the qualitative detection of h^+ production, as shown in Figure 11b. TEMPO exhibits a 1:1:1 signal in analysis and possesses stable chemical properties. The TEMPO molecules combine with the holes to form TEMPOH, which weakens the EPR response, leading to an attenuation of the EPR peak. Thus, the reduction in EPR signal intensity is an indicator for hole generation. Under dark conditions, a more pronounced characteristic peak corresponding to TEMPO-h^+ is observed, whereas under visible light irradiation, a diminished characteristic signal peak indicates participation and consumption of photogenerated holes. This observation confirms the crucial involvement of photogenerated holes in the overall photocatalytic reaction.

During the experiment, real-time absorption spectra of the simulated wastewater containing SEX were measured at various time intervals in order to demonstrate the degradation process of SEX by BTA composites (Figure 11c). Initially, two absorption peaks are clearly observed at 226 and 301 nm, respectively, corresponding to the absorption peak of SEX. After a 20 min period of photocatalytic degradation, the intensity of both peaks decreases, indicating the gradual decomposition and disappearance of SEX during the reaction. As the reaction progresses further, no new absorption peak emerges in the simulated wastewater from mineral processing, and the original peak intensity diminishes. This suggests that both SEX and its intermediate products are broken down into smaller molecules over time.

The absorption peak strength of PL was utilized to characterize the recombination rate of electron–hole pairs. As depicted in Figure 11d, the absorption peak intensity of PL for BTA composites exhibits a tendency to decrease in comparison to BT. This observation suggests that the presence of attapulgite in conjunction with BT leads to a further reduction in the recombination rate of electron–hole pairs. Consequently, a larger number of photogenerated electrons and holes are available to engage in the degradation reaction of xanthate, consequently enhancing the rate of photocatalytic degradation.

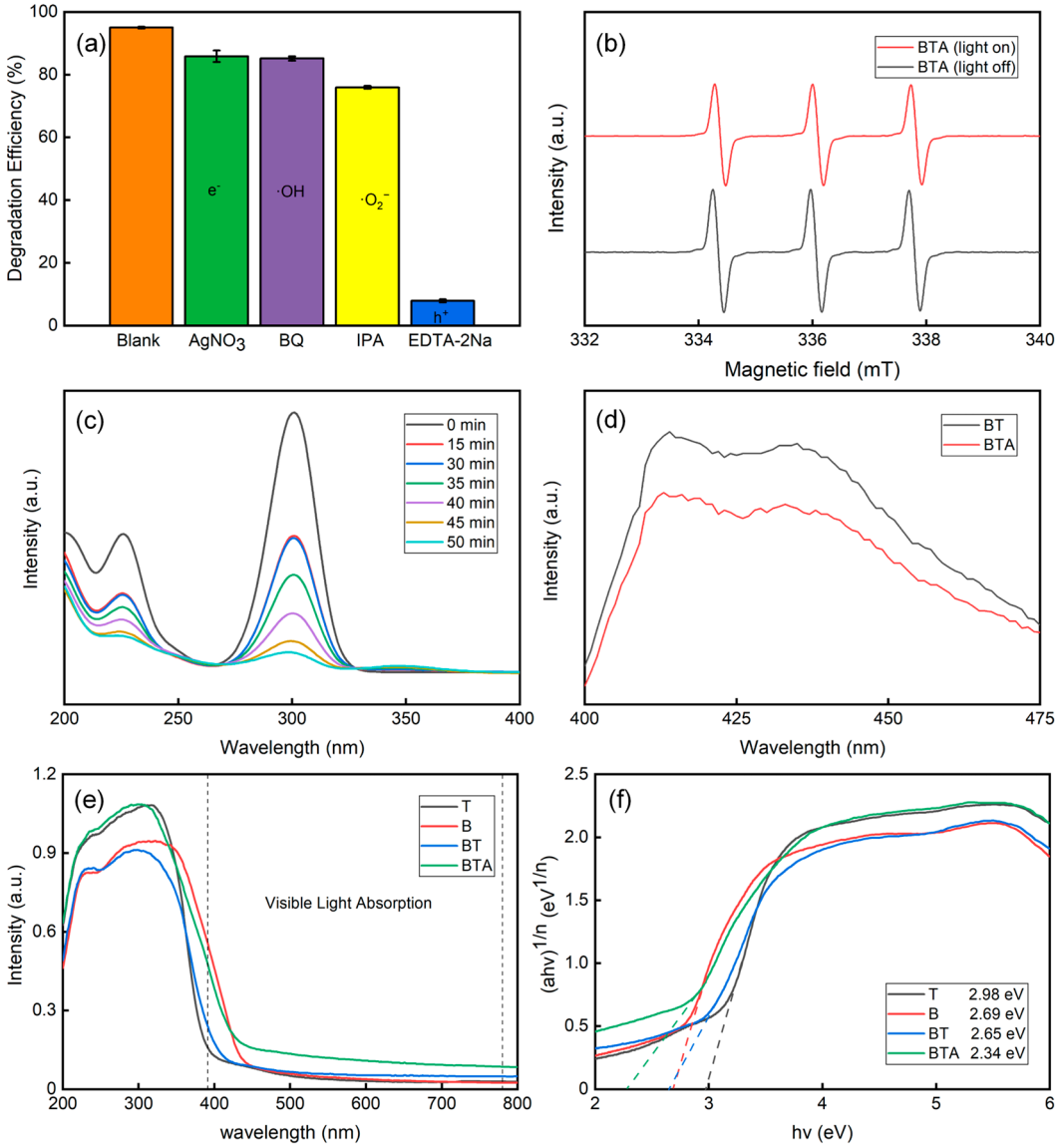

Figure 11. (**a**) Effect of scavenger on the degradation efficiency of SEX. (**b**) EPR spectra of TEMPO-h+. (**c**) Real-time curves of absorbance change of SEX. (**d**) PL spectra. (**e**) UV–vis DRS and (**f**) Bandgaps of different samples.

The photochemical capacity and bandgap energy (E_g) of the as-prepared samples were determined using UV-vis DRS. As shown in Figure 11e,f, it reveals that TiO_2 and BiOBr exhibit absorption edges at 396 and 435 nm, respectively. When the photocatalyst is combined with attapulgite carrier, the optical absorption band edge of BTA composites undergoes a redshift towards longer wavelengths, indicating that the obtained ternary materials significantly enhance their response to visible light, thereby improving the photocatalytic activity. The bandgap widths of different materials were calculated using the Tauc-plot method, as shown in Figure 11f. The bandgap widths for T, B, BT, and BTA are determined to be 2.98, 2.69, 2.65, and 2.34 eV, respectively. BT has a narrower bandgap width compared to TiO_2 and BiOBr due to the generation of a heterojunction. Furthermore, upon loading BT onto attapulgite carrier, BTA exhibits a further decrease in its bandgap to 2.34 eV, implying that the formed composites promote electron–hole pair separation, leading to an increased generation of radical and accelerated degradation reaction rates under visible light irradiation conditions. The valence band potentials (E_{VB}) of TiO_2 and BiOBr are 2.69 and 3.12 eV, respectively [3,43]. Combined with the bandgap width of the

material and the formula of $E_{CB} = E_{VB} - E_g$, the conduction band potentials (E_{CB}) for TiO_2 and BiOBr can be estimated to be −0.29 and 0.43 eV, respectively.

Figure 12 illustrates that the smallest radius of the Nyquist circle is from the BTA sample, suggesting that the BTA ternary composite exhibits reduced charge transfer resistance at the interface, consequently accelerating the photogenerated carrier transfer rate and significantly enhancing the photocatalytic efficiency of BTA.

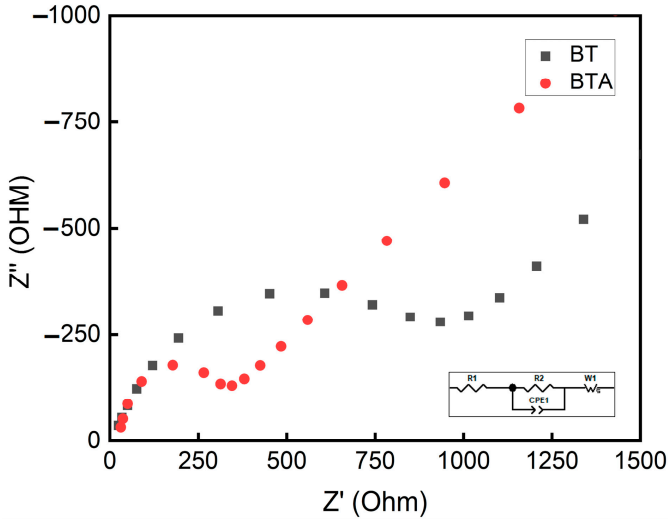

Figure 12. Nyquist EIS plots of different samples.

Based on the microstructural characterization and the photodegradation performance efficiency of the photocatalyst, the corresponding improvement in BTA's ability to harness visible light can be attributed to the heterojunction formation and dispersion of the attapulgite carrier. The enhancement of photocatalytic performance can be attributed to three main reasons: (1) Attapulgite, acting as a carrier, effectively alleviates the agglomeration of TiO_2 and BiOBr and reduces grain size. (2) Attapulgite provides more active adsorption sites and photocatalytic reaction sites for BTA composites, thereby improving the adsorption and catalytic performance of SEX molecules on photocatalysts. (3) The construction of a "type II" heterojunction increases the separation time of photogenerated electron–hole pairs by extending the transport distance of photogenerated carriers, thereby enhancing the photocatalytic reaction activity.

Figure 13 illustrates the degradation mechanism of SEX molecules on the surface of the BTA ternary photocatalyst. After the introduction of attapulgite, SEX is more likely to attach to the reactive active site of BTA composites. Under visible light irradiation, the photogenerated electrons of the TiO_2 conduction band (CB) migrate to the CB of BiOBr due to the lower reduction point of TiO_2. Simultaneously, the photogenerated holes produced by the valence band (VB) in BiOBr transfer to the VB of TiO_2. The migration of photogenerated carriers effectively prevents the recombination of electron–hole pairs, leading to prolonged contact time with SEX molecules and improved photocatalytic efficiency. SEX molecules are initially decomposed into $CH_3O_2S_2^-$, $C_2H_5O_2S_2^-$, $C_2H_5O_2S_2^-$ and $C_4H_5OS_4^-$ under the action of ROS groups dominated by h^+ and supplemented by e^-, ·OH, and $\cdot O_2^-$. Over time, these intermediate products further are decomposed into smaller compounds until they are converted into CO_2, H_2O, SO_4^{2-}, etc.

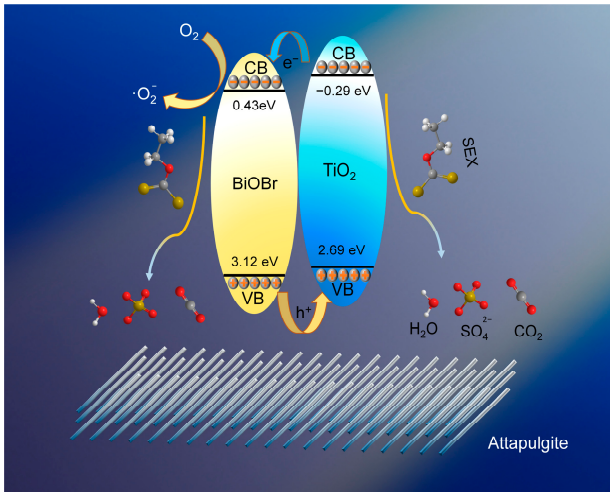

Figure 13. Possible degradation mechanism of SEX under visible light by BTA composites.

3. Materials and Methods

3.1. Materials and Chemicals

Attapulgite was purchased from Changzhou Dingbang mineral products technology Co., Ltd. (Changzhou, China) Sulfuric acid (H_2SO_4, Analytical Reagent, AR), bismuth nitrate pentahydrate ($Bi(NO_3)_3{\cdot}5H_2O$, AR), hydrogen peroxide (H_2O_2, 30%), ammonium hydroxide ($NH_3{\cdot}H_2O$, 25–28%), and potassium bromide (KBr, AR) were purchased from Sinopharm Chemical Reagent Co., Ltd. (Shanghai, China) In addition, Shanghai Macklin Biochemical Co., Ltd. (Shanghai, China) provided the ammonium hexafluorotitanate ($(NH_4)_2TiF_6$, AR). Wuhan Huaxiang Kejie Biotechnology Co., Ltd. (Wuhan, China) and Tieling Flotation Reagents Co., Ltd. (Tieling, China) provided the sodium ethyl xanthate (SEX), sodium butyl xanthate (SBX), sodium isoamyl xanthate (SIAX), and sodium isopropyl xanthate (SIPX). The purity of all xanthates was higher than 85%

3.2. Microstructure Characterization

The crystal phase structure of the samples was observed with X-ray diffraction (XRD, XRD-7000). The morphology of the samples was confirmed by using a scanning electron microscope (SEM, Hitachi S-4800, Tokyo, Japan) and a transmission electron microscope (TEM, JEM-F200, Tokyo, Japan). The surface area of the samples was investigated using the Brunauer–Emmett–Teller method (BET, Quadrasorb SI, Fremont, CA, USA). The thermogravimetric and differential scanning calorimetry (TG-DSC) analysis was investigated by using an analyzer (STA-8000, Waltham, MA, USA). An X-ray photoelectron spectroscope (XPS, NexsaG2, thermo scientific, Waltham, MA, USA) was used to investigate the compositions and valence state of the elements of the obtained composites. Liquid chromatography-mass spectrometry (LC-MS, Agilent 1290 Infinity & Agilent G6125B, Santa Clara, CA, USA) was applied to measure the mass/charge ratio (m/z) to determine the intermediate products.

3.3. Preparation of BiOBr-TiO_2-Attapulgite Composites

This study aimed to synthesize BTA composites using hydrothermal and water-bath methods. Firstly, a 5 wt% H_2SO_4 solution was employed to activate the attapulgite and eliminate impurities. And then, TiO_2-attapulgite (TA) was synthesized through a hydrothermal method, where a mixture of 50 mL of deionized water, 1.5 g of $(NH_4)_2TiF_6$, 4.8 mL of H_2O_2, and some acid-treated attapulgite was stirred at room temperature for 30 min after adjusting the pH to 8 with an ammonia solution. The resulting precursor solution was treated with a hydrothermal reaction at 160 °C for 12 h. Subsequently, the obtained powders underwent repeated washing and drying before being sintered at 400 °C to obtain

TA samples. The samples of acid-treated attapulgite, weighing 0.01 g, 0.1 g, and 1 g, are denoted as TA-1, TA-2, and TA-3, respectively.

Next, BiOBr-TiO_2-attapulgite (BTA) was synthesized using the water-bath method. A mixture of TiO_2-attapulgite and $Bi(NO_3)_3 \cdot 5H_2O$ was stirred and ultrasonicated briefly, and the molar ratio of Ti: Bi was 1:0.05. Then, a KBr solution was dropwise added to maintain a Br:Bi molar ratio of 1:1. After allowing the mixture to react for 2 h at 50 °C, it was washed, dried, and finally subjected to heat treatment at 300 °C to obtain the BiOBr-TiO_2-attapulgite composites. The ternary composites BTA-1, BTA-2 (BTA), and BTA-3 are defined based on the varying inputs of TA-1, TA-2, and TA-3. Similar methods were utilized to synthesize the B, T, and BT samples.

3.4. Measurement of Photocatalytic Activity

The photocatalytic instrument used in this study was a PL-03 infrastructure provided by Beijing Precise Technology Co., Ltd. (Beijing, China) It consists of a circulating cooling system, eight 50 mL quartz tubes, a 400 W xenon lamp, and optical filters. To ensure that the catalytic reaction was not affected by thermal catalysis, the cooling water system maintained a reaction temperature below 20 °C. The xenon lamp served as the visible light source, while the optical filter was used to eliminate ultraviolet light, ensuring that only visible light was emitted. The quartz tubes were used to load different concentrations of the xanthate solution and photocatalysts. Prior to the initiation of the photocatalytic reaction, a 30 min period of dark adsorption was conducted to achieve an adsorption–desorption dynamic equilibrium between the xanthate solution and the photocatalyst using agitation and magnetic stirring. During the dark adsorption and photocatalytic reaction stages, 5 mL of solution was rapidly sampled, and the photocatalyst was filtered to obtain a clear solution using a filter head. Subsequently, the clear solution was analyzed for characteristic peaks using a UV-visible spectrophotometer. The maximum peak of the SEX solution was observed at 301 nm. The relationship between absorbance (A) and mass concentration (C) is shown in Figure S3. As can be observed from the figure, the equation of the standard curve is A = 0.0103 + 0.10032C, R^2 = 0.9988. Therefore, based on the measured absorbance values, the residual concentration of SEX can be determined. The degradation rate (D) can be calculated using the Lambert–Beer law as follows:

$$D = \frac{C_0 - C_t}{C_0} \times 100\% \quad (1)$$

First-order kinetics can be employed to determine the degradation rate of SEX, which can be calculated utilizing the following formula:

$$\ln\left(\frac{C_0}{C_t}\right) = kt \quad (2)$$

Here, C_0 and C_t are the concentrations of SEX solutions at reaction times of 0 and t, respectively. k is the degradation rate constant.

4. Conclusions

The BTA ternary composite photocatalyst was synthesized using a two-step method involving hydrothermal and water-bath routes. Within BTA composites, TiO_2 and BiOBr were uniformly grown, distributed, and coated onto the surface of acid-treated attapulgite, displaying excellent dispersibility and binding properties. The synthesized BTA composites exhibited highly efficient degradation of SEX molecules under visible light conditions within 20 min. The remarkable degradation efficiency of BTA composites could be attributed to the abundant active adsorption and photocatalytic reaction sites provided by attapulgite, as well as the formation of heterojunctions between BiOBr and TiO_2. Through the mechanism of primarily photogenerated holes, the SEX molecules could be converted into CO_2, H_2O, and SO_4^{2-} via possible degradation pathways. BTA composites offer the

advantages of a low production cost, the ability to degrade various xanthates, and excellent recycling performance, thereby demonstrating its potential for treating flotation wastewater. The optimal BTA composites present an efficient, low-energy-consumption, and cost-effective solution for flotation wastewater treatment.

Supplementary Materials: The following supporting information can be downloaded at https://www.mdpi.com/article/10.3390/catal13121504/s1, Figure S1. EDS spectra of BTA composites; Figure S2. LC-MS pattern of SEX after a 5 min photocatalytic reaction; Figure S3. Absorbance standard curve of SEX solution; Table S1. BET specific surface area of different composites; Table S2. Chemical structures and m/z values of possible degradation intermediates of SEX.

Author Contributions: Y.Q.: Conceptualization, Methodology, Investigation, Validation, Visualization, and Writing—original draft. S.Z.: Conceptualization, Methodology, Investigation, Validation, and Funding acquisition. X.J. and Z.K.: Conceptualization and Methodology. S.G. and W.L.: Conceptualization, Methodology, and Supervision. Y.S.: Methodology, Writing—review, Resources, Supervision, and Funding acquisition. All authors have read and agreed to the published version of the manuscript.

Funding: The project was supported by the National Natural Science Foundation of China (52274255, 51674067), National Key R&D Program of China (2020YFB2008702), Fundamental Research Funds for the Central Universities (N2301003, N2201008, N2201004, N2301025), Liaoning Revitalization Talents Program (XLYC1807160), Postdoctoral Foundation of Northeastern University, Young Elite Scientists Sponsorship Program by CAST (2022QNRC001), and China Postdoctoral Science Foundation (2022M720025).

Data Availability Statement: The data presented in this study are available from the corresponding author on request.

Acknowledgments: Special thanks are due to the instrument and data analysis from Analytica and Test Center, Northeastern University.

Conflicts of Interest: The authors declare that they have no known competing financial interest or personal relationships that could have appeared to influence the work reported in this paper.

References

1. Shu, K.; Chuaicham, C.; Noguchi, Y.; Xu, L.; Sasaki, K. In-situ hydrothermal synthesis of Fe-doped hydroxyapatite photocatalyst derived from converter slag toward xanthate photodegradation and Cr(VI) reduction under visible-light irradiation. *Chem. Eng. J.* **2023**, *459*, 141474. [CrossRef]
2. Shen, M.; Zhang, G.; Liu, J.; Liu, Y.; Zhai, J.; Zhang, H.; Yu, H. Visible-light-driven photodegradation of xanthate in a continuous fixed-bed photoreactor: Experimental study and modeling. *Chem. Eng. J.* **2023**, *461*, 141833. [CrossRef]
3. Zhou, P.; Shen, Y.; Zhao, S.; Li, G.; Cui, B.; Wei, D.; Shen, Y. Synthesis of clinoptilolite-supported BiOCl/TiO_2 heterojunction nanocomposites with highly-enhanced photocatalytic activity for the complete degradation of xanthates under visible light. *Chem. Eng. J.* **2021**, *407*, 126697. [CrossRef]
4. Tan, Y.; Chen, T.; Zheng, S.; Sun, Z.; Li, C. Adsorptive and photocatalytic behaviour of PANI/TiO_2/metakaolin composites for the removal of xanthate from aqueous solution. *Miner. Eng.* **2021**, *171*, 107129. [CrossRef]
5. Jia, Y.; Zhang, Y.; Zhang, X.; Cheng, J.; Xie, Y.; Zhang, Y.; Yin, X.; Song, F.; Cui, H. Novel CdS/PANI/MWCNTs photocatalysts for photocatalytic degradation of xanthate in wastewater. *Sep. Purif. Technol.* **2023**, *309*, 123022. [CrossRef]
6. Shen, Y.; Zhou, P.; Zhao, S.; Li, A.; Chen, Y.; Bai, J.; Han, C.; Wei, D.; Ao, Y. Synthesis of high-efficient TiO_2/clinoptilolite photocatalyst for complete degradation of xanthate. *Miner. Eng.* **2020**, *159*, 106640. [CrossRef]
7. Zou, M.; Tan, C.; Yang, H.; Kuang, D.; Nie, Z.; Zhou, H. Facile preparation of recyclable and flexible BiOBr@ TiO_2/PU-SF composite porous membrane for efficient photocatalytic degradation of mineral flotation wastewater. *J. Water Process Eng.* **2022**, *50*, 103127. [CrossRef]
8. Yuan, F.; Zheng, Y.; Gao, D.; Wang, L.; Hu, X. Facile assembly and enhanced visible-light-driven photocatalytic activity of S-scheme BiOBr/g-C_3N_4 heterojunction for degrading xanthate in wastewater. *J. Mol. Liq.* **2022**, *366*, 120279. [CrossRef]
9. Chen, X.; Wang, Z.; Shen, X.; Zhang, Y.; Lou, Y.; Pan, C.; Zhu, Y.; Xu, J. A plasmonic Z-scheme Ag@AgCl/PDI photocatalyst for the efficient elimination of organic pollutants, antibiotic resistant bacteria and antibiotic resistance genes. *Appl. Catal. B Environ.* **2023**, *324*, 122220. [CrossRef]
10. Wei, S.; Kamali, A.R. Trifunctional mesoporous magnetic adsorbent-photocatalyst nanocomposite for efficient removal of potassium ethyl xanthate from mining wastewater. *J. Water Process Eng.* **2022**, *49*, 103067. [CrossRef]
11. Zhou, P.; Shen, Y.; Zhao, S.; Bai, J.; Han, C.; Liu, W.; Wei, D. Facile synthesis of clinoptilolite-supported Ag/TiO_2 nanocomposites for visible-light degradation of xanthates. *J. Taiwan Inst. Chem. Eng.* **2021**, *122*, 231–240. [CrossRef]

12. Shu, K.; Chuaicham, C.; Noguchi, Y.; Xu, L.; Sasaki, K. Charge transfer mechanism through S-scheme heterojunction in in-situ synthesized TiO_2/Fe-doped hydroxyapatite for improved photodegradation of xanthate. *J. Hazard. Mater.* **2023**, *460*, 132337. [CrossRef] [PubMed]
13. Li, G.; Teng, Q.; Sun, B.; Yang, Z.; Liu, S.; Zhu, X. Synthesis scaly Ag-TiO_2 loaded fly ash magnetic bead particles for treatment of xanthate wastewater. *Colloids Surf. A Physicochem. Eng. Asp.* **2021**, *624*, 126795. [CrossRef]
14. Ta, Q.T.H.; Tran, N.M.; Tri, N.N.; Sreedhar, A.; Noh, J.S. Highly surface-active Si-doped TiO_2/$Ti_3C_2T_x$ heterostructure for gas sensing and photodegradation of toxic matters. *Chem. Eng. J.* **2021**, *425*, 131437. [CrossRef]
15. Bott-Neto, J.L.; Martins, T.S.; Oliveira Jr, O.N.; Marken, F. Controlled electrodeposition of brookite TiO_2 for photoelectroanalysis at printed carbon electrodes. *Appl. Surf. Sci.* **2023**, *640*, 158316. [CrossRef]
16. Wang, S.-q.; Li, X.-x.; Wu, J.-j. Preparation of TiO_2/graphene oxide and their photocatalytic properties at room temperature. *J. Fuel Chem. Technol.* **2022**, *50*, 1307–1316. [CrossRef]
17. Meng, Z.; Wang, Y.; Liu, H.; Yan, Y.; Yan, F. Reinforced UHMWPE composites by grafting TiO_2 on ATP nanofibers for improving thermal and tribological properties. *Tribol. Int.* **2022**, *172*, 107585. [CrossRef]
18. Zhou, L.; Yan, Y.; Mao, H.; Zhou, S.; Hui, J.; Li, H.; Li, M.; Zhao, Y.; Zhang, Q.; Xia, S. Development of attapulgite based catalytic membrane for activation of peroxymonosulfate: A singlet oxygen-dominated catalytic oxidation process for sulfamethoxazole degradation. *Sep. Purif. Technol.* **2023**, *312*, 123382. [CrossRef]
19. Yuan, S.; Peng, J.; Zhang, X.; Lin, D.; Geng, H.; Han, B.; Zhang, M.; Wang, H. A mechanically robust slippery surface with 'corn-like' structures fabricated by in-situ growth of TiO_2 on attapulgite. *Chem. Eng. J.* **2021**, *415*, 128953. [CrossRef]
20. Zhang, L.; Zhang, J.; Zhang, W.; Liu, J.; Zhong, H.; Zhao, Y. Photocatalytic activity of attapulgite–BiOCl–TiO_2 toward degradation of methyl orange under UV and visible light irradiation. *Mater. Res. Bull.* **2015**, *66*, 109–114. [CrossRef]
21. Tan, Z.; Zhang, S.; Yue, X.; Zhao, F.; Xi, F.; Yan, D.; Ling, H.; Zhang, R.; Tang, F.; You, K.; et al. Attapulgite as a cost-effective catalyst for low-energy consumption amine-based CO_2 capture. *Sep. Purif. Technol.* **2022**, *298*, 121577. [CrossRef]
22. Zhang, J.; Zhang, L.; Zhou, S.; Chen, H.; Zhong, H.; Zhao, Y.; Wang, X. Magnetically separable attapulgite−TiO_2−Fe O composites with superior activity towards photodegradation of methyl orange under visible light radiation. *J. Ind. Eng. Chem.* **2014**, *20*, 3884–3889. [CrossRef]
23. Cao, W.; Wang, W.; Yang, Z.; Wang, W.; Chen, W.; Wu, K. Enhancing photocathodic protection performance by controlled synthesis of Bi/BiOBr/TiO_2 NTAs Z-scheme heterojunction films. *J. Alloys Compd.* **2023**, *960*, 170675. [CrossRef]
24. Yin, Y.; Kang, X.; Han, B. Two-dimensional materials: Synthesis and applications in the electro-reduction of carbon dioxide. *Chem. Synth.* **2022**, *2*, 19. [CrossRef]
25. Sun, J.; Jiang, C.; Wu, Z.; Liu, Y.; Sun, S. A review on the progress of the photocatalytic removal of refractory pollutants from water by BiOBr-based nanocomposites. *Chemosphere* **2022**, *308*, 136107. [CrossRef] [PubMed]
26. Mao, Y.; Wang, P.; Zhan, S. Shedding light on the role of interfacial chemical bond in heterojunction photocatalysis. *Nano Res.* **2022**, *15*, 10158–10170. [CrossRef]
27. Zhao, S.; Lu, Y.; Lu, R.; Hu, Y.; Rodriguez, R.D.; Chen, J. Constructing BiOBr/TiO_2 heterostructure nanotubes for enhanced adsorption/photocatalytic performance. *J. Water Process Eng.* **2023**, *54*, 103972. [CrossRef]
28. Eskandari, P.; Amarloo, E.; Zangeneh, H.; Rezakazemi, M.; Zamani, M.R.; Aminabhavi, T.M. Photocatalytic activity of visible-light-driven L-Proline-TiO_2/BiOBr nanostructured materials for dyes degradation: The role of generated reactive species. *J. Environ. Manag.* **2023**, *326*, 116691. [CrossRef]
29. Huang, X.; Sun, M.; Humayun, M.; Li, S.; Zhao, J.; Chen, H.; Li, Z. In-situ synthesis of efficient N-graphyne/Bi/BiOBr photocatalysts for contaminants removal and nitrogen fixation. *J. Alloys Compd.* **2023**, *976*, 173025. [CrossRef]
30. Swathi, K.S.; Gopalakrishna Naik, K. Structural, morphological, and optical studies of sol–gel spin coated TiO_2 thin films. *Mater. Today Proc.* **2023**, *960*, 170335. [CrossRef]
31. Zhao, M.; Qin, J.; Wang, N.; Zhang, Y.; Cui, H. Reconstruction of surface oxygen vacancy for boosting CO_2 photoreduction mediated by BiOBr/CdS heterojunction. *Sep. Purif. Technol.* **2024**, *329*, 125179. [CrossRef]
32. Li, B.; Li, L.; Zhang, Q.; Weng, W.; Wan, H. Attapulgite as natural catalyst for glucose isomerization to fructose in water. *Catal. Commun.* **2017**, *99*, 20–24. [CrossRef]
33. Barkouch, H.; Bessbousse, H.; Amar, M.; Bouzzine, S.M.; Hamidi, M.; El Mhammedi, M.A.; Alaoui, O.T. Bismuth-doped TiO_2 enable solar photocatalytic water treatment. *Opt. Mater.* **2023**, *146*, 114507. [CrossRef]
34. Deng, J.; Xu, D.; Zhang, J.; Xu, Q.; Yang, Y.; Wei, Z.; Su, Z. $Cs_3Bi_2Br_9$/BiOBr S-scheme heterojunction for selective oxidation of benzylic C−H bonds. *J. Mater. Sci. Technol.* **2023**, *924*, 166608. [CrossRef]
35. Wu, M.; Zhang, B.; Wang, H.; Chen, Y.; Fan, M.; Dong, L.; Li, B.; Chen, G. Exposed 110 facets of BiOBr anchored to marigold-like $MnCo_2O_4$ with abundant interfacial electron transfer bridges and efficient activation of peroxymonosulfate. *J. Colloid Interface Sci.* **2023**, *653*, 867–878. [CrossRef]
36. Yue, C.; Lin, Y.; Sang, J.; Li, Z.; Zhang, P.; Fan, M.; Leng, Y.; Jiang, P.; Haryono, A. BiOBr/$Bi_{24}O_{31}Br_{10}$ heterojunctions in situ prepared by microwave-assisted hydrothermal method for aerobic oxidation of glycerol to formic acid. *Mater. Today Commun.* **2022**, *31*, 103270. [CrossRef]
37. Zhang, X.; Zhang, J.; Zha, X.; Luo, Y.; Hu, Y.; Chen, G.; He, X. Interfacial chemical bond and oxygen vacancies modulated Mo_2S_3/BiOBr high-low junctions for enhanced photocatalysis gatifloxacin degradation. *Appl. Surf. Sci.* **2023**, *641*, 158548. [CrossRef]

38. Tan, Y.; Yin, C.; Zheng, S.; Di, Y.; Sun, Z.; Li, C. Design and controllable preparation of Bi_2MoO_6/attapulgite photocatalyst for the removal of tetracycline and formaldehyde. *Appl. Clay Sci.* **2021**, *215*, 106319. [CrossRef]
39. Liu, J.; Wang, B.; Liu, W.; Hu, X.; Zhang, C.; Zhou, Z.; Lang, J.; Wu, G.; Zhang, Y.; Yang, J.; et al. Regulating mechanical performance of poly (l-lactide acid) stent by the combined effects of heat and aqueous media. *Int. J. Biol. Macromol.* **2023**, *242*, 124987. [CrossRef]
40. Wang, L.; Wang, T.; Zhang, Y.; Peng, X.; Song, W.; Yang, J.; Yuan, C. Oxidation behaviors of Hongqian heavy crude oil characterized by TG-DSC-FTIR-MS within full temperature regions. *Fuel* **2023**, *353*, 129242. [CrossRef]
41. Zhu, S.-R.; Wu, M.-K.; Zhao, W.-N.; Yi, F.-Y.; Tao, K.; Han, L. Fabrication of heterostructured BiOBr/$Bi_{24}O_{31}Br_{10}$/TiO_2 photocatalyst by pyrolysis of MOF composite for dye degradation. *J. Solid State Chem.* **2017**, *255*, 17–26. [CrossRef]
42. Qi, Y.; Shen, Y.; Zhao, S.; Jiang, X.; Ma, R.; Cui, B.; Zhao, Q.; Wei, D. Degradation of multiple xanthates using highly efficient visible light-responsive BiOBr-TiO_2 composite photocatalysts. *J. Ind. Eng. Chem.* 2023, *in press*. [CrossRef]
43. Shi, Z.; Zhang, Y.; Shen, X.; Duoerkun, G.; Zhu, B.; Zhang, L.; Li, M.; Chen, Z. Fabrication of g-C_3N_4/BiOBr heterojunctions on carbon fibers as weaveable photocatalyst for degrading tetracycline hydrochloride under visible light. *Chem. Eng. J.* **2020**, *386*, 124010. [CrossRef]